

1 Analysis of 3D kinetic simulations of meteor trails

2 **Liane Tarnecki¹and Meers Oppenheim²**

3 ¹Aerospace Engineering Sciences, University of Colorado Boulder, Boulder CO, USA

4 ²Center for Space Physics, Boston University, Boston MA, USA

5 **Key Points:**

- 6 Neutral winds drive the development of waves along trails, particularly when the
7 wind flows perpendicular to the trail and magnetic field.
- 8 Spectra perpendicular to the magnetic field have acoustic-like behaviour moving
9 close to the ion drift speed when a neutral wind is present.
- 10 Waves tend to propagate perpendicular to the magnetic field, with power drop-
11 ping off as a function of aspect angle.

12 **Abstract**

13 Radars detect plasma trails created by the billions of small meteoroids that enter the Earth's
 14 atmosphere daily, returning data used to infer characteristics of the meteoroid popula-
 15 tion and upper atmosphere. Researchers use models to investigate the dynamic evolu-
 16 tion of the trails, enabling them to better interpret radar results. This paper presents
 17 a fully kinetic, 3D code to explore the effects of three trail characteristics: length, neu-
 18 tral wind speed, and ablation altitude. The simulations characterize the turbulence that
 19 develops as the trail evolves and these are compared to radar data. They also show that
 20 neutral winds drive the formation of waves and turbulence in trails, and that wave am-
 21 plitudes increase with neutral wind speed. The finite trail simulations demonstrate that
 22 the bulk motion of the trail flows with the neutral wind. A detailed analysis of simulated
 23 trail spectra yield spectral widths, and evaluate signal strength as a function of aspect
 24 angle. Waves propagate primarily along the length of the trail in all cases, and most power
 25 is in modes perpendicular to \vec{B} . Persistent waves develop at wavelengths corresponding
 26 to the gradient scale length of the original trail. Our results show that the rate at which
 27 power drops with respect to aspect angle in meter-scale modes increases from 5.7 dB/degree
 28 to 6.9 dB/degree with a 15 km increase in altitude. The results will allow researchers
 29 to draw more detailed and accurate information from non-specular radar observations
 30 of meteors.

31 **Plain Language Summary**

32 As meteoroids travel through the atmosphere they leave behind trails of plasma.
 33 The Earth's geomagnetic field and atmospheric winds affect the behaviour of this plasma,
 34 changing the composition and properties of the local environment. We use large-scale
 35 computer simulations that track hundreds of millions of particles to model the evolution
 36 of meteor trails and the large electric fields they generate. This enables us to compare
 37 the effects of changing altitudes, winds, and trail shapes. The simulations show that winds
 38 in the neutral atmosphere drive the formation of waves that travel primarily along the
 39 length of the trail. We can also study the simulated meteors at multiple wavelengths and
 40 angles in order to obtain qualitative estimates of how radars would detect them. The
 41 conclusions drawn from these simulations can be tested by radar observations, and im-
 42 prove our understanding of the physics of meteor trails.

43 **1 Introduction**

44 The Earth's upper atmosphere is constantly bombarded by billions of small me-
 45 teoroids about the size of a grain of sand, moving at speeds greater than 20 km/s, most
 46 invisible to the naked eye. Between 75 and 110 km, meteoroid particles collide with neu-
 47 trals, ionize, and ablate, leaving behind columns of plasma that can stretch tens to hun-
 48 dreds of meters (see Ceplecha et al. (1998) for a review of meteors physics). In the pres-
 49 ence of Earth's geomagnetic field and electric fields that arise in the E-region ionosphere,
 50 these meteor trails develop turbulent waves as they diffuse and cool. Large radars can
 51 measure the characteristics of these trails. This paper presents 3D simulations of the plasma
 52 trails resulting from such meteoroids.

53 Meteors and meteoroids have significant effects on the atmosphere at large scales.
 54 Prior to entering the atmosphere, meteoroids can impact and damage spacecraft. As me-
 55 teoroids ablate, they deposit layers of metallic material measured by numerous optical
 56 instruments and used to track winds in the upper mesosphere and lower thermosphere (Plane
 57 et al., 1999). Meteor metals also modify the chemistry of this region and modify iono-
 58 spheric densities and conductivities, (Ellyett & Kennewell, 1980; Plane, 2004). Dust and
 59 particles left behind seed water clouds (Turco et al., 1982). Characterizing and under-
 60 standing meteors can help researchers mitigate risk to spacecraft and help them observe
 61 and model the upper atmosphere.

62 Meteor observations have been commonly used to study the dynamics of atmospheric
 63 winds and, more recently, temperatures. Assuming that the meteor trails drift with the
 64 neutral winds, the drift speed of the ionized material as observed by the radar is used
 65 as a proxy for the wind velocity (Hocking & Thayaparan, 1997; Hocking, 2001; Kishore
 66 Kumar et al., 2018). These observations are incorporated into large scale atmospheric
 67 models. In the last few years, researchers have begun to use meteor radar estimates to
 68 determine mesospheric temperatures (Lee et al., 2016; Liu et al., 2017; Wen et al., 2014).

69 The majority of meteor data are from radar observations. Large radar arrays like
 70 the Jicamarca Radio Observatory (JRO) detect hundreds to thousands of trails every
 71 hour (Oppenheim et al., 2008). A detailed description of meteor observations with radar
 72 can be found in Chau and Woodman (2004). Optical measurements are possible and pro-
 73 vide a second method for estimating meteor parameters such as mass, but the small me-
 74 teors studied here are difficult to detect optically (Michell et al., 2015, 2019). Rockets
 75 have provided valuable but sparse in situ data with a single detection of an enormous
 76 trail (Kelley et al., 1998).

77 The geometry of a meteor observation effects the data. Specular echoes occur when
 78 the radar beam and the meteor trail are close to perpendicular. This configuration re-
 79 turns a strong signal, and can be observed by small aperture radar. Historically, meteor
 80 radar observed specular trails (Sugar, 1964). Many analysis techniques, including those
 81 described above, rely on specular observations. Non-specular echoes occur when the trail
 82 is approximately perpendicular to the background magnetic field but not the radar beam.
 83 They result from Bragg scattering off field-aligned irregularities in the plasma trail (Chapin
 84 & Kudeki, 1994).

85 Radar observations lend themselves to spectral analysis. Chapin and Kudeki (1994)
 86 shows the time evolution of the spectrum from a single meteor observed at JRO. They
 87 show that a low-Doppler shift peak persists as the trail evolves and develops high-Doppler
 88 shift modes. Many spectra develop asymmetric "wings" of power at high Doppler shift
 89 that gradually disappear. Hall et al. (1997) gives spectral widths for thousands of trails
 90 observed by the SuperDARN network, along with wind and velocity measurements.

91 Close et al. (2008) used observations from ALTAIR to study the relationship be-
 92 tween signal strength and the angle between the trail and the magnetic field (called the
 93 aspect angle). They found that signal strength falls off 3 to 4 dB per degree as the radar
 94 moves away from perpendicular to the magnetic field for ALTAIR's 160 MHz beam. Close
 95 et al. (2008) also investigated signal strength as a function of wavelength. They found
 96 that for non-specular trails, signal strength was proportional to λ^6 , with some altitudi-
 97 nal variation. This roughly agrees with the theoretical prediction in Eshleman (1955)
 98 for short wavelength trails.

99 Radar observations are limited in several ways. Many radar have spatially-fixed ar-
 100 rays and only observe in one direction. This limits the radar to observe at fixed angle
 101 with respect to the Earth's magnetic field. Radar also observe only one wavelength, but
 102 meteor trails generate waves at a wide range of scales.

103 To complement observations, researchers use simulations to explore the 3D struc-
 104 ture and multi-scale modes of meteor trails. Simulations allow researchers to study all
 105 angles and modes present in a trail. The goal of such simulations is to produce predic-
 106 tions that can be tested through observation, and to test physical assumptions about me-
 107 teors and their environment. In conjunction with observations, simulation results can
 108 help researchers interpret results and improve our understanding of meteor evolution.

109 The first fully 3D simulations of meteor trails were published in Oppenheim and
 110 Dimant (2015). They simulated two trails perpendicular to a magnetic field, with and
 111 without an incident neutral wind. Oppenheim and Dimant (2015) found that strong am-
 112 bipolar electric fields caused the formation of plasma ridges along the background mag-

113 netic field. The simulation with no neutral wind developed only low-amplitude waves,
 114 even at the longest timescales. The added wind led to the development of strong waves,
 115 with wavelengths that grew from short to long over the course of the simulation. Trails
 116 in simulations with a neutral wind $\vec{E} \times \vec{B}$ drifted with the background electric and mag-
 117 netic fields. This paper builds on those simulations and introduces new analysis.

118 The simulation methods used in this work are described in Section 2. Sections 3.1
 119 and 3.2 detail the general behaviour of the simulated trails. Various spectral analysis tech-
 120 niques are applied in Section 3.3. The results are discussed in Section 4.

121 2 Simulation Methods

122 Simulations were conducted using EPPIC (Electrostatic Parallel Particle-in-Cell),
 123 the particle-in-cell (PIC) code developed in Oppenheim and Dimant (2004), Oppenheim
 124 and Dimant (2006), and Oppenheim and Dimant (2013), among others. This electro-
 125 static PIC code is well suited to modeling this problem, as it capture all kinetic processes
 126 including particle heating and Landau damping of waves. EPPIC simulates fully kinetic,
 127 collisional plasmas using ion and electron macroparticles, and can include externally im-
 128 posed electric and magnetic fields E_0 and B_0 .

129 The simulated plasma consists of several billion ions and electrons (see Birdsall and
 130 Langdon (1985) for a full treatment of PIC methods). EPPIC allows collisions with neu-
 131 trals, which have a uniform background density. All collisions in EPPIC are electron-
 132 neutral or ion-neutral, where the probability of a collision is proportional to the macropar-
 133 ticle's velocity. There are no Coulomb or neutral-neutral collisions. A more complete de-
 134 scription of the collision mechanism can be found in Oppenheim and Dimant (2004).

135 Like all kinetic PIC codes, this method requires some adjustment of physical pa-
 136 rameters for numerical efficiency. Notably, the electron mass is artificially inflated to 44
 137 times the true value (Oppenheim & Dimant, 2013). Background parameters closely mimic
 138 those in Oppenheim and Dimant (2015) For computational efficiency, the background
 139 density has a lower value than one would likely find naturally. Oppenheim and Dimant
 140 (2015) extensively tested these adjustments to ensure that simulations using these more
 141 efficient parameters produce similar results to far more expensive runs using more phys-
 142 ically accurate parameters. The simulations in this work were tested with multiple back-
 143 ground densities, with only marginal differences in outcome. All simulations use the same
 144 parameters, except where noted. See Table 1 for a list of simulation parameters.

145 The simulations presented here use a more efficient field solver than that in Oppenheim
 146 and Dimant (2015). This rapid spectral technique, based on the p3dfft package (Pekurovsky,
 147 2019), requires periodic boundary conditions in all directions. Effectively, this means that
 148 the simulation box is surrounded by identical boxes. For a meteor simulation, this ef-
 149 fect is physically equivalent to an infinite number of meteors laid out on a grid. The di-
 150 mensions must be carefully chosen to avoid contact between the meteor and its 'neigh-
 151 bors'. Unfortunately, it is impossible to avoid contact in all directions, due to the mo-
 152 bility of electrons along magnetic field lines. The dimension along B is made as large as
 153 feasible given computational resources, but complete isolation of the trail is impossible.

154 The geometry of a trail is as follows. The trail extends along the \vec{x} axis, and a mag-
 155 netic field of $\vec{B} = 0.5$ G points along the \vec{z} axis. \vec{B} points perpendicular to the column
 156 of the trail, and lies along the longest dimension of the simulation. Dimant et al. (2009)
 157 and Dimant and Oppenheim (2006) explored the effect on the plasma fields and drifts
 158 of changing the alignment of \vec{B} with respect to the trail. They found that the behav-
 159 ior does not significantly differ unless the magnetic field and the trail are nearly par-
 160 allel, and otherwise simply scales with the sine of the angle between the trail and the field.
 161 These simulations represent the physics of both non-specular trails when examining the
 162 spectra perpendicular to B ($k_z \approx 0$) and specular trails when examining the spectra

Table 1. Simulation parameters.

Parameter	Value
B_z	0.5 G
Background plasma density	100 cm ⁻³
Peak plasma density	1200 cm ⁻³
Simulation electron mass	44m _e
Grid cell size	0.05 × 0.05 × 0.05 m
Box Size	25.6 × 25.6 × 102.4 m
Neutral temperature	300 K
Time step	1.25 × 10 ⁻⁶ s

163 perpendicular to the trail ($k_x = 0$). The initial trail consists of a smooth, thermalized
 164 plasma column in a neutral background. The peak column density is 120 times the back-
 165 ground neutral density of 100 cm⁻³, and falls off as a Gaussian with a variance of 0.8
 166 m. As the computational cost of each simulation increases with plasma density, this den-
 167 sity value was selected as a compromise between a more realistic, denser plasma and a
 168 simulation that would complete in a reasonable amount of time. The Gaussian column
 169 is a reasonable assumption for the shape of the thermalized plasma trail, but the verac-
 170 ity of this claim is investigated with models of meteoroid ablation and trail formation
 171 in other work (Sugar et al., 2018).

172 Applying an electric field $\vec{E} = \vec{u} \times \vec{B}$ moves the simulation into the frame of ref-
 173 erence of a neutral wind \vec{u} . Simulations with a neutral wind apply a 5 mV/m electric
 174 field \vec{E}_0 directed along the trail (\vec{x}), corresponding to a 100 m/s wind in the $-\hat{y}$ direc-
 175 tion. Note that because the frame transformation used places the simulation in the frame
 176 of the neutral wind, the whole simulation box can be thought of as moving with the wind
 177 and any motion inside the box as in addition to this bulk motion.

178 Two trail-end geometries are tested. The trail either extends across the entire box,
 179 or falls off exponentially at the edges. These edge conditions respectively produce effec-
 180 tively infinitely long trails and short, finite segments. Further discussion on the phys-
 181 icality of these simulations appears in the following section.

182 In order to simulate meteors at different altitudes, the collision rates for ion-neutral
 183 and electron-neutral collisions are adjusted. In this case, both collision rates are reduced
 184 by one e-folding, corresponding to an increase in altitude of about a scale height. Our
 185 baseline run approximates conditions at 100 km, and a second, otherwise identical run,
 186 approximates collision rates found at 115 km. While only two altitudes are tested in this
 187 work, additional cases can be explored in future work.

188 3 Results

189 Oppenheim and Dimant (2015) presented the first 3D kinetic PIC simulations of
 190 meteor trails. In this paper, those simulations are improved and the effects of varying
 191 three simulation parameters are explored: trail-end geometry, neutral wind speed, and
 192 altitude. The spectra perpendicular to and off of \vec{B} of the simulated trails are examined
 193 in order to evaluate signal strength as a function of wavelength and field alignment.

194 The simulation box is 512 x 512 x 2048 grid cells, with a grid cell size of 0.05 me-
 195 ters in all directions. Thus, the entire box extends 25.6 x 25.6 x 102.4 meters. These sim-
 196 ulations improve upon the resolution of those in Oppenheim and Dimant (2015) by a fac-
 197 tor of two. Each simulation time step is 1.25 μ s for 31200 steps, for a 39 ms total sim-

198 ulation. Each simulation runs for over 15 hours on 4096 processors using the Stampede
 199 2 supercomputer.

200 **3.1 Trail evolution**

201 In all cases trails diffuse quickly at the beginning of the simulation. Most of this
 202 initial diffusion occurs along \vec{B} , due to the mobility of electrons along the magnetic field,
 203 and the same formation of plasma ridges noted in Oppenheim and Dimant (2015) is ob-
 204 served. Waves develop in all cases, though amplitudes are small in cases with no neu-
 205 tral wind. To the eye, the most prominent mode is $\lambda = 2-3$ m. Waves typically form
 206 with small amplitudes, then grow. Without a neutral wind, waves quickly reach a max-
 207 imum amplitude, but with a wind the amplitude continues to grow for the duration of
 208 the simulation time. The physical extent of the waves can sometimes grow to the scale
 209 of the trail width, resulting in some fracturing of the main body of the trail.

210 Figure 1 shows the evolution of ion density in the plane perpendicular to \vec{B} in a
 211 simulation with a 100 m/s neutral wind. The simulation resolution is 5 cm in all dimen-
 212 sions, reduced for output to 10 cm. In simulations with no neutral wind, waves form on
 213 both sides of the trail in the plane perpendicular to both the trail and \vec{B} (the xy plane).
 214 Recall that the simulation is in the frame of reference of the neutral wind, so the bulk
 215 motion of the trail is with the wind. The plasma waves that form within the trail tend
 216 to propagate in the $-\vec{x}$ direction on the top side of the trail, and in the $+\vec{x}$ direction on
 217 the bottom side. The introduction of a neutral wind breaks the symmetry and causes
 218 waves not to develop on the bottom side of the trail, and have larger amplitudes and more
 219 turbulence on the top side. For a neutral wind vector \vec{u} , turbulence tends to develop where
 220 $\vec{u} \parallel \nabla n$.

221 In the following discussion, “turbulence” refers to the plasma waves that form and
 222 propagate along the trail; these structures are not equivalent to any of the drivers large-
 223 scale neutral turbulence in the mesosphere and thermosphere, such as gravity waves (Fritts
 224 & Lund, 2011). Such phenomena occur at larger physical scales than are considered in
 225 these simulations.

226 The simulations with a neutral wind tend to $\vec{E} \times \vec{B}$ drift in the $-\vec{y}$ direction. Real
 227 trails likely do not $\vec{E} \times \vec{B}$ drift, and stay instead with the neutral wind. This assump-
 228 tion is tested by modifying the trail-end geometry in Section 3.2. Note that, as real trails
 229 extend through regions in which neutral winds change dramatically, a single trail can be
 230 carried along at different speeds along its length. These results explore only uniform wind
 231 fields at two neutral wind speeds. However, additional simulations have shown that the
 232 relationship between neutral wind speed and turbulence is as expected. Faster neutral
 233 winds drive stronger turbulence that develops faster, but do not appear to trigger sig-
 234 nificantly different phenomena.

235 **3.2 Finite trail simulations**

236 In Oppenheim and Dimant (2015), periodic boundary conditions create a trail of
 237 effectively infinite length. The trail extends along the entire simulation box, and par-
 238 ticles and fields wrap from one side of the system to the other. This is a non-physical
 239 geometry, and can prevent the development of ambipolar electric fields within the trail.
 240 To test the effect of finite trail edges, several simulations in which the density of the trail
 241 falls off exponentially at the ends of the trail were run, creating a short segment of plasma.
 242 Due to computational constraints, the main body of these simulated trails is only 15 me-
 243 ters long, and density falls off over an additional 5 meters on each end. Meteors in na-
 244 ture are comparatively larger, and can reach up to tens of kilometers in length (Dimant
 245 et al., 2009; Sugar et al., 2018). However, the plasma density along real trails likely varies
 246 due to differential ablation or fracturing of the meteoroid. Periodic boundary conditions

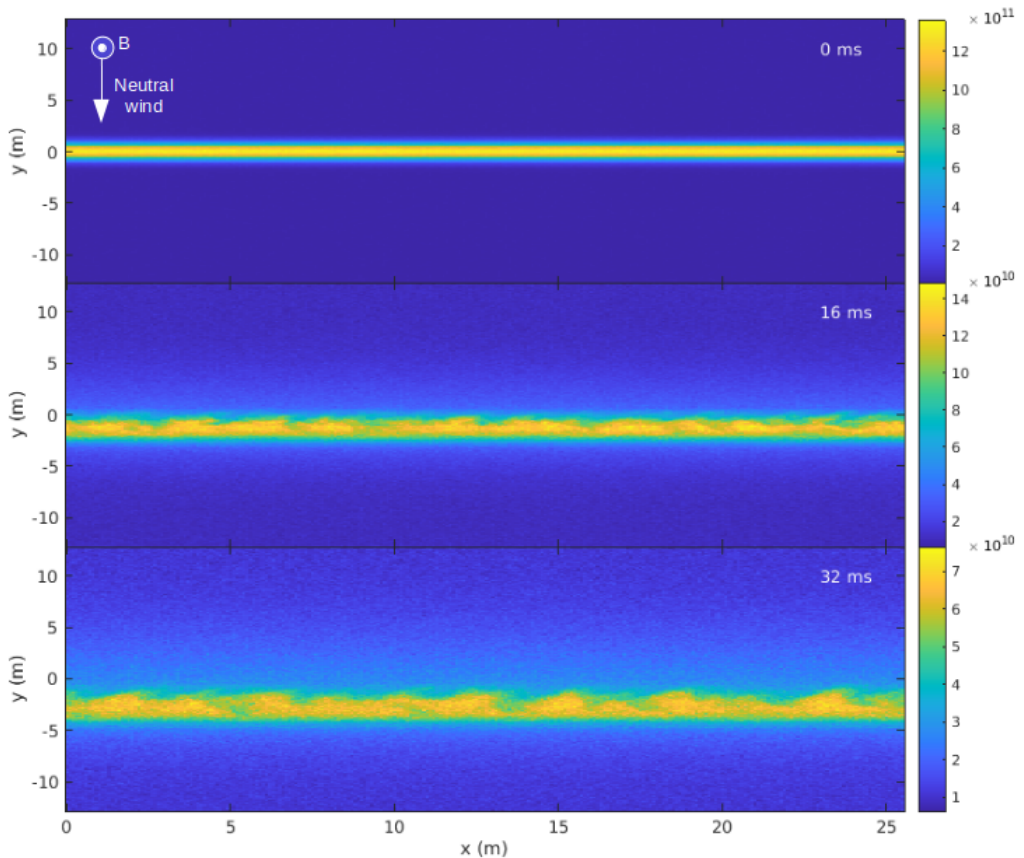


Figure 1. Ion density evolution of an infinite-trail simulation at 100 km with an incident neutral wind of 100 m/s. Cuts are through the center of the trail in the xy-plane, and \vec{B} points out of the page. Density is in m^{-3} . Movie included in supplementary information.

247 on these simulations also effectively create an array of short trail segments. A truly ac-
 248 curate simulation of real meteors lies somewhere between segmented and infinite trails
 249 presented here.

250 The finite trails show a few differences in evolution from the infinite simulations.
 251 In the these simulations, waves develop first near the ends of the trail, then propagate
 252 toward the center. Figure 2 shows that in simulations with incident neutral winds, the
 253 ends of the trail often deform and bend away from the rest of the trail. Notably, trails
 254 with finite edges follow the neutral wind, rather than $\vec{E}_0 \times \vec{B}$ drifting as infinite trails
 255 do. Particles moving along \vec{E}_0 build up at the edges of the trail, leading to a build up
 256 of charge that introduces a polarization electric field \vec{E}_{pol} directed anti-parallel to \vec{E}_0 .
 257 $\vec{E}_{pol} \times \vec{B}$ pulls the trail in the positive \hat{y} direction and works against the $\vec{E}_0 \times \vec{B}$ drift.
 258 Importantly, the trail then generally moves with the neutral wind. This supports the as-
 259 sumption made when deriving neutral wind speeds from meteor radar, as discussed in
 260 Section 1. Notably, the infinite trails do not drift strictly with the neutral wind, but have
 261 an additional drift in the $-\hat{y}$ direction. The finite trails also have an additional drift in
 262 the $-\hat{x}$ direction, anti-parallel to E_0 . This drift is caused by an asymmetry in the po-
 263 larization electric field that leads to an average electric field in the $-\hat{x}$ direction. Waves
 264 also develop slightly sooner in finite trail simulations. However, these changes have lit-
 265 tle impact on the evolution and behavior of the trails as a whole. Once waves have de-
 266 veloped fully finite and infinite trails behave similarly, and spectra from finite trails do
 267 not differ significantly from those of infinitely long trails.

268 These results indicate that infinite trails capture the same general behavior and
 269 physics as the finite trails, with the exception of the $\vec{E} \times \vec{B}$ drift noted above. The fi-
 270 nite trail simulations deserve further consideration, especially as computers improve and
 271 larger physical scales can be achieved, but at this time they provide little additional in-
 272 sight. As the finite trail segments are more likely to introduce numerical complications
 273 to the simulation (due to communication between "neighboring" segments), all further
 274 discussion in this paper concerns only infinite simulations, unless otherwise noted.

275 3.3 Spectral analysis

276 The 3D simulations allow the extraction of measurable spectral quantities compa-
 277 rable to radar observations. The meteor trail power spectra as a function of frequency
 278 and wavenumber and the rate of power decay as a function of angle off of $\perp \vec{B}$ are ex-
 279 plored.

280 3.3.1 Spectra perpendicular to \vec{B}

281 Power spectra are useful indicators of the types of wave modes that develop in the
 282 simulation. Because 4D spectra (k_x, k_y, k_z, ω) can be difficult to work with, slices of spec-
 283 tral space are selected. The mobility of electrons along the magnetic field works to short
 284 out the formation of waves in this direction, so the spectra perpendicular to $\perp \vec{B}$ are
 285 particularly emphasized.

286 Figure 3 shows the evolution of the spectrum perpendicular to \vec{B} for the simula-
 287 tion with a wind. The spectra show four stages. At $t=0$, the spectrum of the body of
 288 the trail appears as a sharp peak at $k_x = 0$. This peak persists throughout the simu-
 289 lation, though it drops in amplitude and broadens through the run as the trail diffuses.
 290 To better display the spectra of the developing waves, the maximum power displayed in
 291 Figure 3 is capped at 85 dB. Turbulence first develops with peak power around $k_x =$
 292 5 m^{-1} , corresponding to 1.3 m wavelengths. As the simulation continues, the peak spec-
 293 tral power shifts to smaller k , plateauing near $k_x = 2 \text{ m}^{-1}$, corresponding to 3 m wave-
 294 lengths.

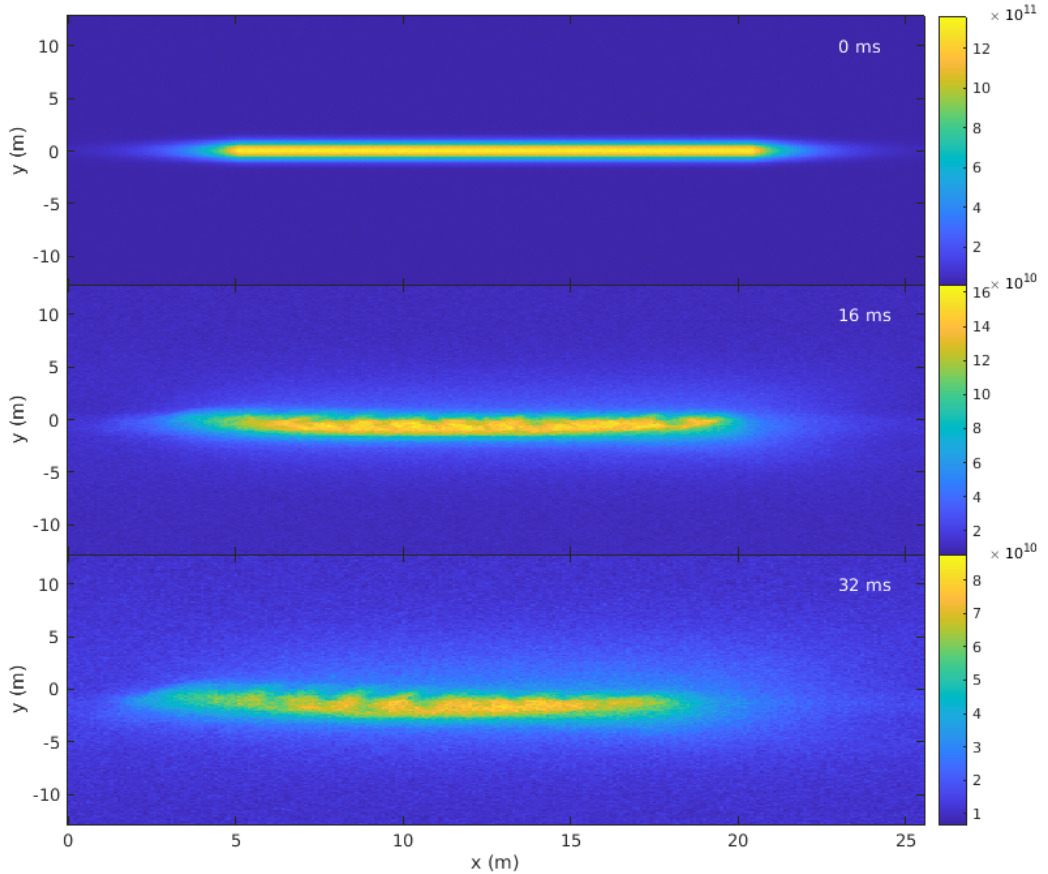


Figure 2. Ion density evolution of a finite-trail simulation at 100 km with an incident neutral wind of 100 m/s. Cuts are in the plane perpendicular to \vec{B} and through the center of the trail. Note that the ends of the trail are deformed as the simulation progresses, and the trail as a whole drifts in the direction of the neutral wind. Video included in supplementary information.

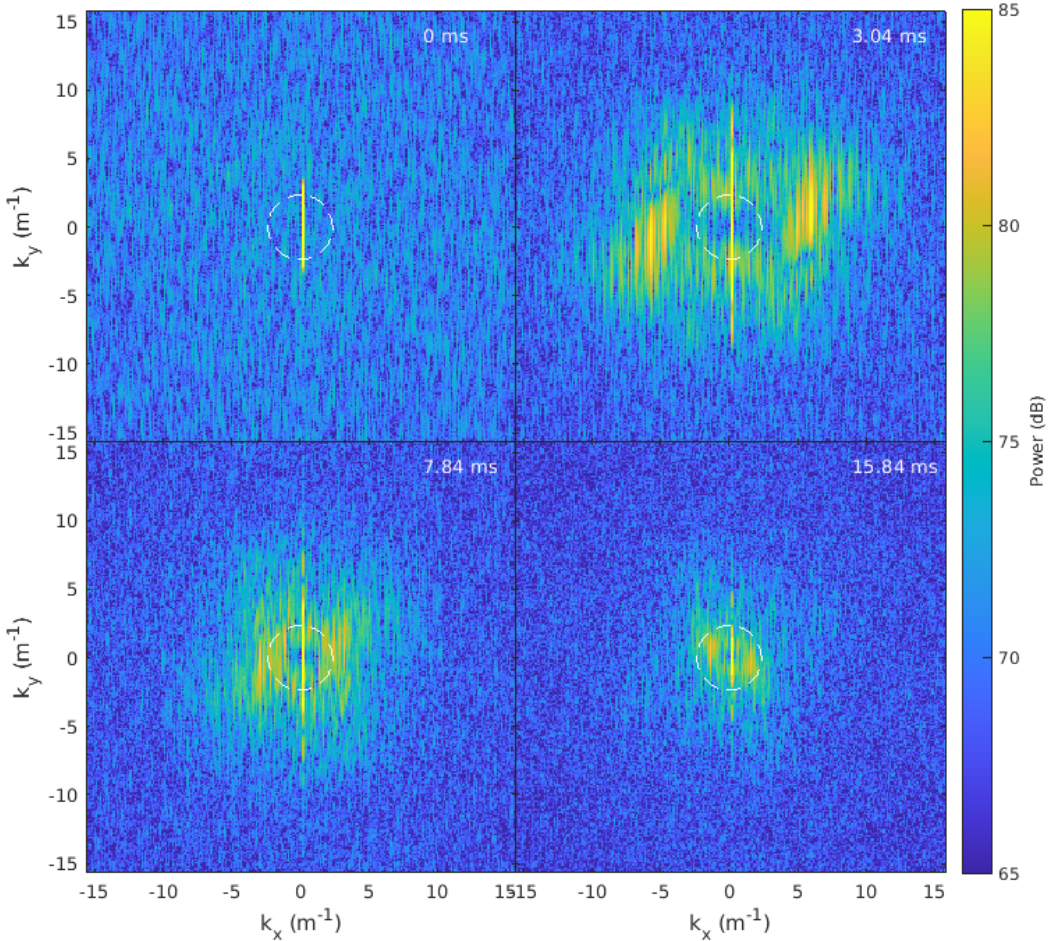


Figure 3. Power spectra, $P(k_x, k_y, k_z = 0)$, over time for a simulation with a 100 m/s neutral wind. A narrow peak at $k_x = 0$ corresponds to the overall structure of the trail. Power develops at large k and shifts to smaller k over the course of the simulation. The wavenumber of the maximum gradient length scale at the beginning of the simulation (7 m) is indicated by the dashed white circle.

The gradient scale length ($L = n_0/\nabla n_0$) perpendicular to the initial trail distribution ranges from 2 to 7 meters over the steepest part of the gradient. The wavenumber of 7 m modes is indicated as a dashed circle in Figure 3. Once the turbulence is well developed, the majority of the spectral power lies in or around this circle. This coincides with the theory of the gradient drift instability, which predicts that the dominant wavelength is about the gradient scale length (Huba & Lee, 1983). Note that as the trail diffuses the gradient length scale increases.

Modes with $k_y = k_z = 0$ are representative of some of the strongest modes in the system, corresponding to waves travel along the trail (in the \vec{x} direction). Figures 4 and 5a show $k_x - \omega$ spectra for meteors with and without incident neutral winds. These spectra are generated from the ion distribution after the turbulence is well developed. The spectra show acoustic-like modes with roughly $\omega \propto k$. In the simulation with no neutral wind, the spectrum shows modes moving in both the positive and negative \vec{x} directions, while waves in the simulation with a neutral wind show modes traveling only in the positive \vec{x} direction. Their power exceeds the no-wind amplitude by more than

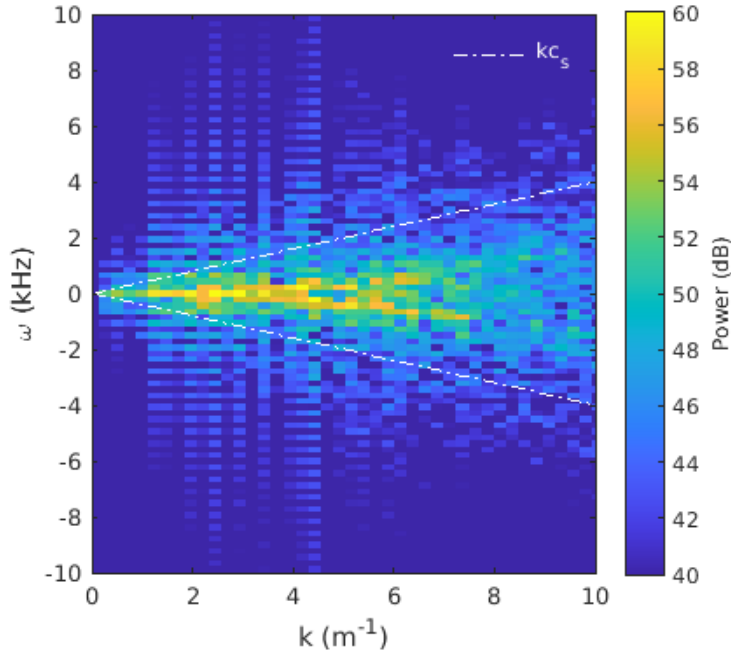


Figure 4. Spectrum of modes with $k_y = k_z = 0$ for a simulation without an incident neutral wind at 100 km. The dashed lines correspond to the ion thermal speed.

10 dB, making the waves in the other direction invisible. This agrees with our qualitative analysis of the wave behavior. These spectra also show which modes have the most power along the trail. Visually, the dominant mode is 3 meter waves. The spectra show a broad distribution of power between $k = 2$ and $k = 6 \text{ m}^{-1}$ (1 to 3 meter waves), peaking around $k = 3 \text{ m}^{-1}$. Spectral power begins to fall off at wavenumbers greater than $k = 6 \text{ m}^{-1}$, and drops entirely into the noise regime for $k > 8 \text{ m}^{-1}$. The initial power drop-off is approximately linear with wavelength; however, this is not necessarily a physical effect and further simulations are necessary to fully explore the wavelength dependence.

Figures 4 and 5a also indicate the ion thermal speed (c_s) for both simulations, and the ion drift velocity (v_d) corresponding to the background electric and magnetic fields for the simulation with a neutral wind. The peak spectral power appears to obey the dispersion relation $\omega = k_x v_d$ in the presence of a neutral wind. In both cases, peak power appears to be bounded by $k c_s$.

Figure 5b shows the spectrum for a run 15 km higher in altitude than that in Figure 5a, but is otherwise identical. The peak power in the spectrum shifts slightly from $k = 1-3 \text{ m}^{-1}$ to $k = 3-5 \text{ m}^{-1}$ with the change in altitude. The changes in the spectra at higher altitude are due to multiple physical processes. As altitude increases, the background neutral density decreases exponentially. This increases the ion mean free path, which allows the ions of the trail to diffuse faster at higher altitudes and prevents shorter wavelength modes from forming. However, cross-field electron mobility decreases with altitude as the magnetized electrons are tied to field lines. The electrons thus cannot easily follow the diffusing ions, leading to separation of charges and the development of an ambipolar electric field that drives the formation of waves. The developing turbulence is then the mechanism for transporting electrons across \vec{B} .

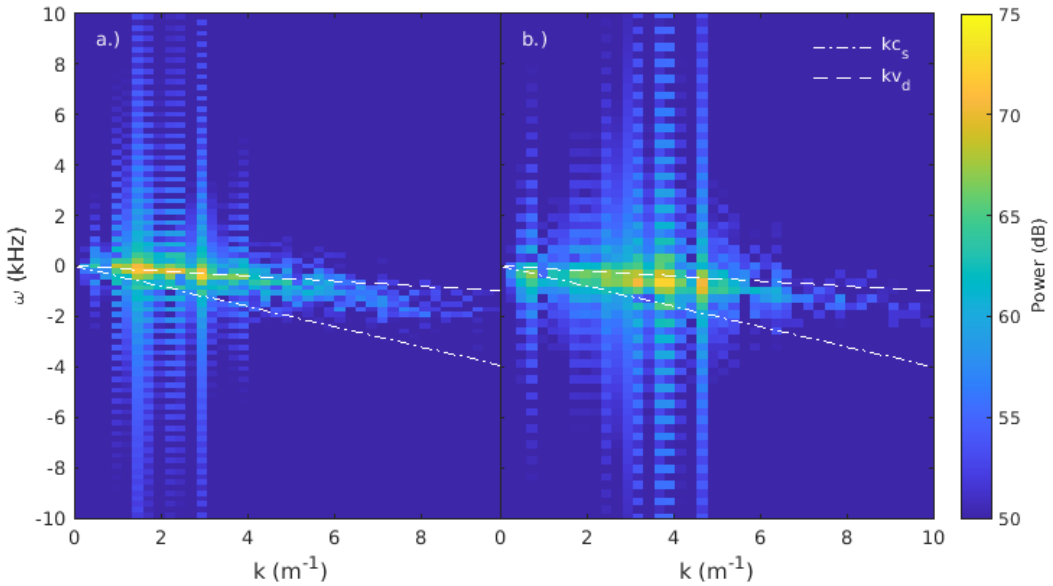


Figure 5. Spectra of modes with $k_y = k_z = 0$ for a simulation with an incident neutral wind at a.) 100 km and b.) 115 km. The dashed and dotted lines correspond to the ion drift velocity due to the background electric and magnetic fields and the ion thermal speed.

335 Spectral widths can also be derived from these spectra. Figure 6 shows spectra at
 336 single wavenumbers along the trail for simulations with and without a neutral wind at
 337 100 and 115 km. In both cases, the spectra broaden and skew at higher wavenumbers.
 338 At smaller wavenumbers ($0.2\text{-}4.6\text{ m}^{-1}$) the spectra at higher altitude are broader, and
 339 vice versa at larger wavenumbers ($7.1\text{-}9.6\text{ m}^{-1}$).

340 3.3.2 Spectral power off perpendicular to \vec{B}

341 In the simulations, waves propagate primarily along the trail, perpendicular to \vec{B} .
 342 The following analysis selects individual wavenumbers and investigates spectral power
 343 as a function of angle off of $\perp \vec{B}$ (aspect angle). 3 meter modes are analyzed here, cor-
 344 responding with the observing frequency of the Jicamarca radar. The power at small an-
 345 gles off \vec{B} are of particular interest, as one might expect power to fall off quickly with
 346 aspect angle.

347 To study spectral power as a function of angle, the Fourier transform of ion den-
 348 sity is interpolated to a grid as a function of \vec{k} and aspect angle, then average over the
 349 frequency dimension. The aspect angles are rescaled by a factor corresponding to the
 350 inflated electron mass, to account for increased mobility along \vec{B} . Since the perpendic-
 351 ular electron mobility is inversely dependent on m_e ($g_{e\perp}^{Ped} \approx \nu_{ene}e/(m_e\Omega_e^2)$, $g_{e\perp}^H = e/(m_e\Omega_e)$),
 352 PIC electrons have artificially reduced mobility. The angles reported here are rescaled
 353 to account for this (see Dimant and Oppenheim (2006)). The selection is restricted to
 354 later times in the simulation, once waves have developed fully. All simulation variants
 355 produce qualitatively similar results. Figure 7 shows the results for simulations with and
 356 without neutral winds at 100 and 115 km. Most power is along the trail, perpendic-
 357 ular to \vec{B} . The power in any given wavenumber falls off as a function of aspect angle, as
 358 electron mobility along \vec{B} shorts out waves, until the signal is indistinguishable from the
 359 noise level in the simulation. However, the presence of a neutral wind significantly af-
 360 fects the relationship with aspect angle. Without a neutral wind, waves develop only at

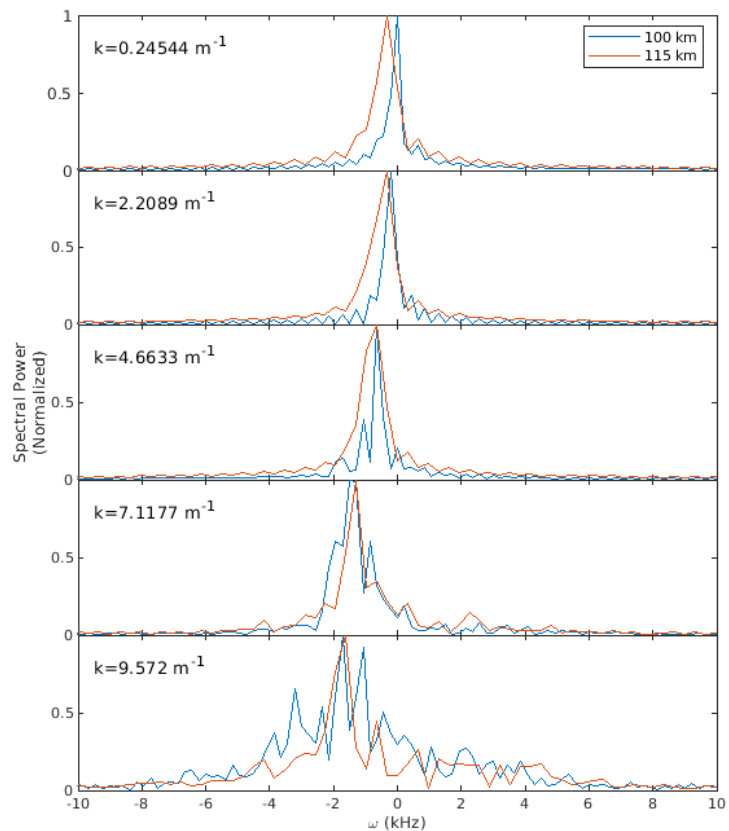


Figure 6. Normalized spectra for two simulations with a 100 m/s neutral wind, at 100 (blue) and 115 km (red). Spectra are perpendicular to \vec{B} at various wavelengths.

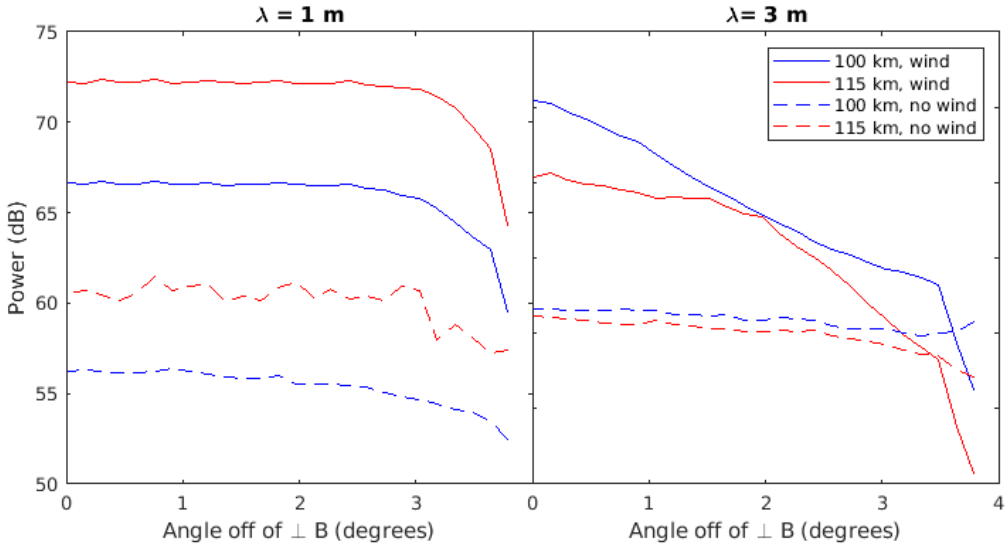


Figure 7. Spectral power in $\lambda = 1, 3$ m modes ($k \approx 6, 2 \text{ m}^{-1}$) as a function of angle off perpendicular to \vec{B}_0 for simulations with (solid lines) and without (dashed lines) a neutral wind. Angles have been rescaled to adjust for artificially reduced electron mobility along \vec{B} .

small amplitudes and without much power, even strictly perpendicular to \vec{B} . Therefore, spectral power is more distributed as a function of aspect angle.

In general, total spectral power is greater at 115 km than 100 km. At $\lambda = 3$ m, power falls off slightly faster at 115 km ($\approx 6.9 \text{ dB/degree}$) than at 100 km ($\approx 5.7 \text{ dB/degree}$). At $\lambda = 1$ m the behaviour is qualitatively different. Spectral power is relatively constant for several degrees, then falls off sharply. This is an unexpected result, as radar have previously observed power in 1 m waves dropping off as a function of aspect angle (see 4), and the $k - \omega$ spectra in Figure 5 show that there is some power at 1 m, though less than at 3 m.

4 Discussion & Conclusions

In this paper, a parallel PIC technique is used to model 3D meteor trails under a variety of conditions. Our simulations provide two observable quantities for radars: power as a function of aspect angle and spectral width. While the literature contains little data about the former, as most radar have a fixed angle with respect to \vec{B} , a few theoretical and observational studies have been made. Close et al. (2008), using the ALTAIR radar, observed that radar signal strength falls of 3 to 4 dB per degree off of perpendicular to \vec{B} at 160 MHz (1.87 meters) for non-specular trails over a range of 6° off perpendicular to \vec{B} . However, Close et al. (2008) used data from just six trails in this analysis, spread over more than 20 degrees of aspect angle and 35 km altitude. While the overall trend is, as reported, a power loss of 3-4 dB per degree, there is enough variation between the data points that the trend may be close to constant at some ranges. Zhou et al. (2004) used numerical simulations to investigate the aspect sensitivity of meteoric field-aligned irregularities, and found that power dropped about 10 dB every 6° , or over 1.5 dB per degree. Our simulations agree more closely with the results from Close et al. (2008), but do not necessarily contradict the results in Zhou et al. (2004). More data from observations and simulations must be collected to draw further conclusions. The simulations are also limited to very small meteors and larger, more realistic ones may develop narrower spectra.

389 Haldoupis and Schlegel (1993) noted that meteor echoes can have both narrow and
 390 broad Doppler spectrum widths, and that the spectral width of an individual trail varies
 391 over time. Hall et al. (1997) report spectral widths of several thousand meteor trails ob-
 392 served with the Saskatoon SuperDARN radar. They find that meteor trails have extremely
 393 narrow spectral widths, on the order of a few to tens of meters per second. These find-
 394 ings are corroborated in Milan et al. (2001) and Arnold et al. (2001). Arnold et al. (2001)
 395 found that spectra broadened with increasing altitude (on the order of 1 m/s per kilo-
 396 meter), and attributed this result to the loss of weak signals at lower altitudes. They also
 397 noted an inverse relationship between returned power and spectral width for the same
 398 reason. To summarize, they observed high-power, narrow spectra at low altitudes, and
 399 weaker, broader spectra at higher altitudes. Bourdillon et al. (2005) observed spectra
 400 that are broad at onset, then narrow as the signal decays. In contrast, Chapin and Kudeki
 401 (1994) shows meteor spectra that broaden over time. In general, the literature reports
 402 much narrower spectra than these simulations produce, by at least an order of magni-
 403 tude. These spectral widths are generally the result of specular observations. L. P. Dyrud
 404 et al. (2004) report observations of hundreds of non-specular trails, with average spec-
 405 tral widths of about 100 m/s. These results are in better agreement with the simulations.
 406 The difference between the spectra of specular and non-specular trails can be better ex-
 407 plored in future work. With increased computing power, simulating many meteors and
 408 averaging the resulting spectra could be a valuable tool to reduce the significant simu-
 409 lation noise present in the simulated spectra.

410 As the simulations presented in this work place no constraints on the alignment
 411 of meteor with respect to the ground or to a theoretical radar observer, the results ap-
 412 ply to both specular and non-specular trails. L. Dyrud et al. (2012) show that the fea-
 413 tures of non-specular echoes can be explained by plasma instabilities in the trail. These
 414 simulations show that when the trail is perpendicular to \vec{B} , the usual geometry for non-
 415 specular echoes, plasma waves form readily in the presence of a neutral wind. Non-specular
 416 echoes have also been observed for trails at angles far from perpendicular to the mag-
 417 netic field (Chau et al., 2014). This phenomenon has been attributed to dusty plasma
 418 resulting from large boloids (Kelley et al., 1998), while the meteors in this work con-
 419 sist of relatively pure plasmas resulting from small meteoroids.

420 As discussed in Section 3, plasma turbulence only develops in simulations that in-
 421 clude a neutral wind. These results agree with previous simulations, which show that
 422 neutral winds drive plasma turbulence in meteor trails, and that a trail that is not in
 423 the presence of a neutral wind should develop little to no turbulence (L. Dyrud et al.,
 424 2011). However, observational studies show that real trails develop turbulence even with-
 425 out a neutral wind; this discrepancy is as-yet unexplained (Oppenheim et al., 2009). In
 426 the future, we plan to explore the effects of neutral wind sheers on the development of
 427 turbulence and waves in order to understand why trails in regions of slow changing winds
 428 still seem to show clear evidence of plasma irregularities. Additionally, these simulations
 429 consider only neutral winds directed perpendicular to the trail. We suspect that com-
 430 ponents of the neutral wind parallel to the trail will have relatively little impact on the
 431 plasma dynamics, as they will simply cause the electrons and ions to travel with the wind
 432 and will not induce any appreciable electric fields or currents.

433 This analysis leaves much work left to be done. As computing facilities improve,
 434 more extensive simulations can be performed, increasing box size and resolution as well
 435 as approaching the true parameters of the physical system. Even with existing compu-
 436 tational abilities, this work leaves a broad parameter space unexplored. The effects of
 437 altitude and neutral wind speed on spectra can be investigated with more resolution, as
 438 well as additional parameters not included in this work such as peak trail density, tem-
 439 perature, and neutral wind sheer. Improving the physicality of the simulations and in-
 440 vestigating the effect of varying additional parameters will improve our theoretical un-
 441 derstanding of the system and provide better comparisons to observational data.

442 Simulations of short trail “segments” show that the trail tends to drift with the neu-
 443 tral wind, as one would expect. Neutral winds also stimulate the growth of turbulence;
 444 without a neutral wind, only small amplitude waves develop. Spectral analysis shows that
 445 waves develop first at short wavelengths, then grow to longer wavelengths. Most wave
 446 power develops between $k = 2$ and $k = 6 \text{ m}^{-1}$. This indicates that the instability is
 447 gradient-driven. If a neutral wind is present, the peak spectral power tends to follow the
 448 dispersion relation $\omega = kv_d$, where v_d is the ion drift speed due to external fields. Spec-
 449 tral power is also concentrated perpendicular to \vec{B} , and falls off as a function of aspect
 450 angle. Finally, spectra broaden and skew as a function of wavenumber. These results im-
 451 prove our theoretical understanding of the evolution of meteor trails, and can be used
 452 to compare to radar observations.

453 Acknowledgments

454 This work was supported by NSF grant ATM-1007789 and NASA award NNx11AO96G.
 455 Computation was performed using the TACC computational facility at University of Texas
 456 at Austin, supported by NSF grant AcI-1053575, and with the Shared Computing Clus-
 457 ter at Boston University. The source code and input files used to produce the simula-
 458 tions in this work are archived at <http://doi.org/10.5281/zenodo.4252708>. Simulation
 459 outputs are archived on the TACC Stampede 2 system; TACC account holders who wish
 460 to access this data directly should contact the corresponding author.

461 References

462 Arnold, N., Robinson, T., Lester, M., Byrne, P., & Chapman, P. (2001, 04). Super
 463 dual auroral radar network observations of fluctuations in the spectral
 464 distribution of near range meteor echoes in the upper mesosphere and lower
 465 thermosphere. *Annales Geophysicae*, 19. doi: 10.5194/angeo-19-425-2001

466 Birdsall, C. K., & Langdon, A. B. (1985). *Plasma physics via computer simulation*.
 467 McGraw-Hill, New York.

468 Bourdillon, A., Haldoupis, C., Hanuise, C., Roux, Y. L., & Menard, J. (2005). Long
 469 duration meteor echoes characterized by doppler spectrum bifurcation. *Geo-
 470 phys. Res. Lett.*, 32. doi: 10.1029/2004GL021685

471 Ceplecha, Z., Borovička, J., Elford, W. G., Revelle, D. O., Hawkes, R. L., Porubčan,
 472 V., & Šimek, M. (1998, September). Meteor Phenomena and Bodies. , 84,
 473 327-471. doi: 10.1023/A:1005069928850

474 Chapin, E., & Kudeki, E. (1994). Plasma wave excitation on meteor trails in the
 475 equatorial electrojet. *Geophys. Res. Lett.*, 21. doi: 10.1029/94GL01705

476 Chau, J. L., Strelnikova, I., Schult, C., Oppenheim, M. M., Kelley, M. C., Stober,
 477 G., & Singer, W. (2014). Nonspecular meteor trails from non-field-aligned
 478 irregularities: Can they be explained by presence of charged meteor dust?
 479 *Geophysical Research Letters*, 41(10), 3336-3343. doi: 10.1002/2014GL059922

480 Chau, J. L., & Woodman, R. F. (2004). Observations of meteor-head echoes us-
 481 ing the jicamarca 50mhz radar in interferometer mode. *Atmospheric Chemistry
 482 and Physics*, 4(2), 511–521. doi: 10.5194/acp-4-511-2004

483 Close, S., Hamlin, T., Oppenheim, M., Cox, L., & Colestock, P. (2008). Depend-
 484 ence of radar signal strength on frequency and aspect angle of nonspecular
 485 meteor trails. *Journal of Geophysical Research: Space Physics*, 113(A6). doi:
 486 10.1029/2007JA012647

487 Dimant, Y., & Oppenheim, M. (2006). Meteor trail diffusion and fields: 1. simu-
 488 lations. *Journal of Geophysical Research: Space Physics*, 111(A12). doi: 10
 489 .1029/2006JA011797

490 Dimant, Y., Oppenheim, M. M., & Milikh, G. M. (2009). Meteor plasma trails: ef-
 491 fects of external electric field. *Annales Geophysicae*, 27(1), 279–296. doi: 10
 492 .5194/angeo-27-279-2009

493 Dyrud, L., Oppenheim, M., Close, S., & Hunt, S. (2012). Interpretation of
 494 non-specular radar meteor trails. *Geophys. Res. Lett.*, *29*. doi: 10.1029/
 495 2002GL015953

496 Dyrud, L., Urbina, J., Fentzke, J. T., Hibbit, E., & Hinrichs, J. (2011). Global vari-
 497 ation of meteor trail plasma turbulence. *Annales Geophysicae*, *29*(12), 2277–
 498 2286. doi: 10.5194/angeo-29-2277-2011

499 Dyrud, L. P., Denney, K., Close, S., Oppenheim, M., Chau, J., & Ray, L. (2004).
 500 Meteor velocity determination with plasma physics. *Atmospheric Chemistry
 501 and Physics*, *4*(3), 817–824. doi: 10.5194/acp-4-817-2004

502 Ellyett, C., & Kennewell, J. (1980). Radar meteor rates and atmospheric density
 503 changes. *Nature*, *287*. doi: 10.1038/287521a0

504 Eshleman, V. R. (1955). Theory of radio reflections from electron-ion clouds. *Trans-
 505 actions of the IRE Professional Group on Antennas and Propagation*, *3*(1),
 506 32–39.

507 Fritts, D. C., & Lund, T. S. (2011). Gravity wave influences in the thermo-
 508 sphere and ionosphere: Observations and recent modeling. In M. A. Abdu &
 509 D. Pancheva (Eds.), *Aeronomy of the earth's atmosphere and ionosphere* (pp.
 510 109–130). Dordrecht: Springer Netherlands. doi: 10.1007/978-94-007-0326-1_8

511 Haldoupis, C., & Schlegel, K. (1993). A 50-mhz radio doppler experiment for mid-
 512 latitude e region coherent backscatter studies: System description and first
 513 results. *Radio Science*, *28*(06), 959–978. doi: 10.1029/93RS01373

514 Hall, G. E., MacDougall, J. W., Moorcroft, D. R., St.-Maurice, J.-P., Manson, A. H.,
 515 & Meek, C. E. (1997). Super dual auroral radar network observations of
 516 meteor echoes. *Journal of Geophysical Research: Space Physics*, *102*(A7),
 517 14603–14614. doi: 10.1029/97JA00517

518 Hocking, W. K. (2001). Middle atmosphere dynamical studies at resolute bay over a
 519 full representative year: Mean winds, tides, and special oscillations. *Radio Sci-
 520 ence*, *36*(6), 1795–1822. doi: 10.1029/2000RS001003

521 Hocking, W. K., & Thayaparan, T. (1997). Simultaneous and colocated obser-
 522 vation of winds and tides by mf and meteor radars over london, canada
 523 (43° n, 81° w), during 1994–1996. *Radio Science*, *32*(2), 833–865. doi:
 524 10.1029/96RS03467

525 Huba, J. D., & Lee, L. C. (1983). Short wavelength stabilization of the gradient drift
 526 instability due to velocity shear. *Geophysical Research Letters*, *10*(4), 357–360.
 527 doi: 10.1029/GL010i004p00357

528 Kelley, M., Alcala, C., & Cho, J. (1998). Detection of a meteor contrail and mete-
 529 oric dust in the earth's upper mesosphere. *Journal of Atmospheric and Solar-
 530 Terrestrial Physics*, *60*(3), 359 – 369. doi: 10.1016/S1364-6826(97)00113-2

531 Kishore Kumar, G., Nesse Tyssøy, H., & Williams, B. P. (2018). A preliminary com-
 532 parison of na lidar and meteor radar zonal winds during geomagnetic quiet and
 533 disturbed conditions. *Journal of Atmospheric and Solar-Terrestrial Physics*,
 534 *168*, 70–79. doi: doi.org/10.1016/j.jastp.2018.01.010

535 Lee, C., Kim, J.-H., Jee, G., Lee, W., Song, I.-S., & Kim, Y. H. (2016). New
 536 method of estimating temperatures near the mesopause region using meteor
 537 radar observations. *Geophysical Research Letters*, *43*(20), 10,580–10,585. doi:
 538 10.1002/2016GL071082

539 Liu, L., Liu, H., Le, H., Chen, Y., Sun, Y.-Y., Ning, B., ... Xiong, J. (2017). Meso-
 540 spheric temperatures estimated from the meteor radar observations at mohe,
 541 china. *Journal of Geophysical Research: Space Physics*, *122*(2), 2249–2259. doi:
 542 10.1002/2016JA023776

543 Michell, R., DeLuca, M., Janches, D., Chen, R., & Samara, M. (2019). Simulta-
 544 neous optical and dual-frequency radar observations of small mass meteors
 545 at arecibo. *Planetary and Space Science*, *166*, 1–8. doi: doi.org/10.1016/
 546 j.pss.2018.07.015

547 Michell, R., Janches, D., Samara, M., Hormaechea, J., Brunini, C., & Bibbo, I.

548 (2015). Simultaneous optical and radar observations of meteor head-echoes
 549 utilizing saamer. *Planetary and Space Science*, *118*, 95 - 101. (SI:ACM Inter-
 550 related) doi: doi.org/10.1016/j.pss.2015.04.018

551 Milan, S., Lester, M., Sato, N., & Takizawa, H. (2001, 02). On the altitude de-
 552 pendence of the spectral characteristics of decametre-wavelength e region
 553 backscatter and the relationship with optical auroral forms. *Annales Geophysicae*, *19*. doi: 10.5194/angeo-19-205-2001

555 Oppenheim, M., & Dimant, Y. (2004). Ion thermal effects on e-region instabilities:
 556 2d kinetic simulations. *Journal of Atmospheric and Solar-Terrestrial Physics*,
 557 *66*(17), 1655 - 1668. (40 Years of Equatorial Aeronomy Sparked by the Jica-
 558 marca Radio Observatory) doi: doi.org/10.1016/j.jastp.2004.07.007

559 Oppenheim, M., & Dimant, Y. (2006). Meteor induced ridge and trough formation
 560 and the structuring of the nighttime e-region ionosphere. *Geophysical Research
 561 Letters*, *33*(24). doi: 10.1029/2006GL028267

562 Oppenheim, M., & Dimant, Y. (2013). Kinetic simulations of 3-d farley-buneman
 563 turbulence and anomalous electron heating. *Journal of Geophysical Research
 564 (Space Physics)*, *118*, 1306-1318. doi: 10.1002/jgra.50196

565 Oppenheim, M., & Dimant, Y. S. (2015). First 3-d simulations of meteor plasma dy-
 566 namics and turbulence. *Geophysical Research Letters*, *42*(3), 681-687. doi: 10
 567 .1002/2014GL062411

568 Oppenheim, M., Sugar, G., Bass, E., Dimant, Y. S., & Chau, J. (2008). Day
 569 to night variation in meteor trail measurements: Evidence for a new the-
 570 ory of plasma trail evolution. *Geophysical Research Letters*, *35*(3). doi:
 571 10.1029/2007GL032347

572 Oppenheim, M., Sugar, G., Slowey, N. O., Bass, E., Chau, J. L., & Close, S. (2009).
 573 Remote sensing lower thermosphere wind profiles using non-specular meteor
 574 echoes. *Geophysical Research Letters*, *36*(9). doi: 10.1029/2009GL037353

575 Pekurovsky, D. (2019). P3DFFT: a framework for parallel computations of
 576 fourier transforms in three dimensions. *CoRR*, *abs/1905.02803*. doi:
 577 10.1137/11082748X

578 Plane, J. (2004). A time-resolved model of the mesospheric na layer: constraints on
 579 the meteor input function. *Atmospheric Chemistry and Physics*, *4*(3), 627-638.
 580 doi: 10.5194/acp-4-627-2004

581 Plane, J., Cox, R., & Rollason, R. (1999). Metallic layers in the mesopause
 582 and lower thermosphere region. *Advances in Space Research*, *24*(11),
 583 1559-1570. (Ionospheric/Thermospheric/Mesospheric Coupling) doi:
 584 10.1016/S0273-1177(99)00880-7

585 Sugar, G., Oppenheim, M. M., Dimant, Y. S., & Close, S. (2018). Formation of
 586 plasma around a small meteoroid: Simulation and theory. *Journal of Geophys-
 587 ical Research: Space Physics*, *123*(5), 4080-4093. doi: 10.1002/2018JA025265

588 Sugar, G. R. (1964). Radio propagation by reflection from meteor trails. *Proceedings
 589 of the IEEE*, *52*(2), 116-136. doi: 10.1109/PROC.1964.2801

590 Turco, R., Toon, O., Whitten, R., Keesee, R., & Hollenbach, D. (1982). Noc-
 591 tilucent clouds: Simulation studies of their genesis, properties and global
 592 influences. *Planetary and Space Science*, *30*(11), 1147-1181. doi: 10.1016/
 593 0032-0633(82)90126-X

594 Wen, Y., Jin-Song, C., Chun-Bo, M., Na, L., & Zhen-Wei, Z. (2014). Observation
 595 of upper atmospheric temperature by kunming all-sky meteor radar. *Chinese
 596 Journal Of Geophysics*, *57*(8), 2423. doi: 10.6038/cjg20140804

597 Zhou, Q., Morton, Y. T., Mathews, J. D., & Janches, D. (2004). Aspect sensi-
 598 tivity of vhf echoes from field aligned irregularities in meteor trails and thin
 599 ionization layers. *Atmospheric Chemistry and Physics*, *4*(3), 685-692. doi:
 600 10.5194/acp-4-685-2004